OPTICA

# Enhanced penetration depth in optical coherence tomography and photoacoustic microscopy *in vivo* enabled by absorbing dye molecules

David A. Miller,[1,†] Yirui Xu,[1,†] Robert Highland,[1] Van Tu Nguyen,[1] William J. Brown,[2] Guosong Hong,[3,4] Junjie Yao,[1,5] and Adam Wax[1,*]

[1]Department of Biomedical Engineering, Duke University, Durham, North Carolina 27708, USA
[2]Lumedica Vision Inc., Durham, North Carolina 27701, USA
[3]Department of Materials Science and Engineering, Stanford University, Stanford, California 94305, USA
[4]Wu Tsai Neurosciences Institute, Stanford University, Stanford, California 94305, USA
[5]junjie.yao@duke.edu
[†]These authors contributed equally to this work.
*a.wax@duke.edu

Received 31 October 2024; revised 5 December 2024; accepted 10 December 2024; published 8 January 2025

**The scattering and absorption of light within biological tissue severely limits the penetration depth of optical imaging techniques. Recently, it has been found that water-soluble, strongly absorbing dye molecules, such as tartrazine, can achieve *in vivo* tissue transparency by increasing the refractive index of aqueous components in tissue, as predicted by the Lorentz oscillator model and Kramers–Kronig relations. In this study, we topically applied absorbing dye molecules to the abdominal skin of pigmented and nonpigmented mice to enhance the penetration depth of optical coherence tomography (OCT) and photoacoustic microscopy (PAM). In both types of mice, the penetration depth of OCT was significantly improved using tartrazine and 4-aminoantipyrine. As predicted by the Kramers–Kronig relations and absorption spectra of the dyes, mice treated with 4-aminoantipyrine showed significantly improved penetration depth compared to mice treated with tartrazine for the PAM system with 532 nm excitation. These findings further demonstrate the use of absorbing dye molecules for achieving tissue transparency to enhance the penetration depth of depth-resolved optical imaging modalities in skin, thus accelerating the translation of these technologies in clinical areas, such as dermatology.** 

https://doi.org/10.1364/OPTICA.546779

## 1. INTRODUCTION

The penetration depth of optical imaging methods is limited by the scattering and absorption of light within biological tissues [1,2]. Light scattering in tissue arises from the refractive index (RI) difference between low RI, aqueous components and high RI, lipid and protein components. Optical clearing agents (OCAs) reduce this RI difference by either replacing the aqueous components with higher RI substances or by removing high RI lipids and proteins. However, tissue clearing with traditional OCAs may require the use of cytotoxic chemicals or the removal of water and lipids, which make them unsuitable for longitudinal *in vivo* imaging [3–5]. Prior work has explored the use of OCAs, such as glycerol, propylene glycol, glucose, and polyethylene glycol, for achieving *in vivo* tissue transparency [2]. However, these OCAs may introduce side effects, such as tissue dehydration, that have significant drawbacks for *in vivo* imaging [6,7].

Recently, Ou *et al*. demonstrated that water-soluble, strongly absorbing dye molecules with a narrow absorption peak achieve reversible optical transparency in tissue by increasing the RI of the aqueous components within the tissue [6]. Using the Lorentz oscillator model the authors predicted that dye molecules with sharper absorption resonances at wavelengths less than the imaging wavelength effectively increase the real component of the RI of the aqueous medium at the imaging wavelength, as predicted by the Kramers–Kronig relations. Thus, absorbing dye molecules, such as tartrazine, can reduce RI contrast in tissue to achieve transparency. Many of these dyes are common food dyes approved by the US Food and Drug Administration. In their report, Ou *et al*. thoroughly demonstrate the use of this novel tissue clearing technique to noninvasively visualize gut motility using bright-field and fluorescence imaging, sarcomeres using second-harmonic generation microscopy, and brain vasculature using laser speckle imaging. However, the benefits of this novel optical clearing approach have yet to be explored in depth-resolved optical imaging modalities.

Optical coherence tomography (OCT) is an optical imaging technique that uses low-coherence interferometry to noninvasively capture high-resolution, 3D images of biological tissues [8–10]. OCT serves as an optical biopsy, which has led to the rapid adoption of OCT by ophthalmologists for characterizing the structure of the retina, where tissue biopsy is nearly impossible without

disrupting function. In other specialties, such as dermatology, the adoption of the technology has been slower due to the high degree of optical scattering by tissues like the skin [11,12]. Previous studies have used conventional OCAs, such as glycerol or polypropylene glycol, to improve the penetration depth of OCT in tissues [7,13]. However, the use of absorbing dyes for enhancing OCT penetration depth has yet to be explored. Photoacoustic microscopy (PAM) combines laser-induced ultrasound waves with optical absorption contrast to produce high-resolution images [14]. Like OCT, PAM also faces challenges in achieving deep tissue imaging due to light scattering and attenuation, limiting its depth penetration to less than 1 mm in skin [15]. Conventional OCAs, such as glycerol, have also been explored for enhancing penetration depth of PAM for *ex vivo* and *in vivo* imaging [16,17].

In this report, we seek to build on the work by Ou *et al*. by demonstrating the use of absorbing dye molecules for enhancing the penetration depth of depth-resolved optical imaging modalities. First, we used OCT to compare the penetration depth enhancement in the skin of pigmented and nonpigmented mice after topical application of 4-aminoantipyrine (380 nm absorbance peak) and tartrazine (428 nm absorbance peak). Next, we used OCT to track the time course of penetration depth enhancement after topical dye application. Lastly, we used ultrafast PAM to visualize vasculature beneath the mouse abdominal skin before and after treatment with 4-aminoantipyrine and tartrazine.

## 2. METHODS

### A. Optical Coherence Tomography

OCT imaging was performed using a portable commercial OCT system (Labscope 3.0, Lumedica, Durham, NC). This system featured a center wavelength of 840 nm with 110 nm bandwidth to achieve an axial resolution of 2.8 μm in air. A 4× objective was used throughout this study to achieve a lateral resolution of 15 μm. Images were captured using a 2048-pixel array at an A-line rate of 80 kHz. OCT images were captured in line scan mode consisting of 30 repeated B-scans with a 1 mW illumination power. After acquisition, raw OCT images were processed following traditional spectral domain OCT processing, including background normalization, *k*-space interpolation, dispersion compensation, and fast Fourier transform. Processed B-scan stacks were registered and averaged 10 times for analysis. Each B-scan was 3 mm along the axial dimension and 3.5 mm along the transverse dimension.

### B. Ultrafast Photoacoustic Microscopy

PAM was performed using an ultrafast photoacoustic microscopy (UF-PAM) system, as depicted in Fig. S1. A green pulsed laser with a wavelength of 532 nm, operating at a frequency of 1 MHz and power of 200 mW, serves as the excitation source. A rotating polygon mirror operating in air provides rapid line scanning at a speed of 2.4 kHz. A customized cylindrical ultrasound transducer (UT) is used to record the PA signals. The transducer has an open window in the center, enabling confocal alignment between the laser line beam and the ultrasound focus. The polygon mirror facilitates fast scanning along the $x$ axis, while a stepper motor moves the sample along the $y$ axis for 3D image formation. An FPGA (myrio1900, National Instruments) synchronizes the laser, polygon mirror, and motorized stage. PA signals are amplified using preamplifiers (ZFL-500LN+, Minicircuits) and digitized by a 250 MHz digitizer (ATS9350, AlazarTech). PAM images were captured over a 12 mm × 12 mm area with a maximum penetration depth of 1 mm. The UF-PAM system has a lateral resolution of 10 μm and axial resolution of 73.5 μm.

### C. Animal Preparation

All animal imaging was performed in compliance with the Duke University Institutional Animal Care and Use Committee. We imaged two healthy, male (18 g and 21 g) C57BL/6 black mice and one pregnant, female (56 g) CD-1 mouse. Mice were anesthetized using 5% isoflurane with supplemental oxygen at a flow rate of 1.5 L/min. The abdomen of each mouse was shaved using an electric trimmer and treated with Nair to remove the remaining fur. After treating with Nair for 5 minutes, the abdomen was cleaned using isopropyl alcohol pads. During imaging, mice were maintained under anesthesia using 1%–3% isoflurane with supplemental oxygen and their body temperature was regulated using a heating pad.

### D. Dye Preparation

Gel compounds of each dye for topical application were prepared by mixing low melting temperature agarose with different dye solutions. First, the dye powder was dissolved in 1XPBS (38% w/w 4-aminoantipyrine or 30% w/w tartrazine). Next, the dye solution was preheated in an 80 C water bath before combining with agarose to reach a final agarose concentration of 10 mg/mL. The solution was then removed from the water bath and cooled in a 4°C refrigerator. After cooling for 10 min, the solution formed a clear orange gel that remained stable at room temperature for at least 4 h.

### E. Dye Application

Gel solutions containing the dye (4-aminoantipyrine or tartrazine) were mixed with pumice particles as needed, and a thin topical coating of the solution was massaged onto the bare mouse skin using a cotton tip applicator for 10 min until the pink skin turned to red (color of concentrated dye). After this time, the pumice particles were wiped away and pure gel solution was applied until maximum tissue transparency was achieved (∼3−5 min). After imaging was complete, the dye was removed by rinsing the skin with warm water or saline until the skin returned to normal. Neosporin was applied after rinsing and drying skin to prevent skin infection.

## 3. RESULTS

We topically applied 4-aminoantipyrine and tartrazine to the abdominal skin of live pigmented and nonpigmented mice. Figure 1 depicts the pigmented mouse abdominal skin before [Fig. 1(a)] and after applying 4-aminoantipyrine [Fig. 1(b)] and tartrazine [Fig. 1(c)] in separate experiments. Prior to tissue clearing, only the surface of the bare skin is visible to the naked eye. Within 5 min of applying the optical clearing solutions, structures beneath the skin surface became visible to the naked eye, including blood vessels and internal organ structures. Visual inspection revealed the pigmented mouse treated with 4-aminoantipyrine displayed a more dramatic tissue clearing effect [Fig. 1(b)] than the mouse treated with tartrazine [Fig. 1(c)]. The mouse treated with

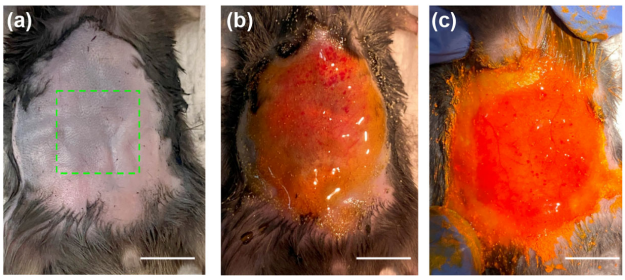


**Fig. 1.** Mouse abdomen before (a) and after applying 4-aminoantipyrine (b) and tartrazine (c). Dashed green box in (a) indicates region in which OCT and PAM imaging were performed. Scale bar: 1 cm.

tartrazine weighed 21 g, suggesting the mouse likely had more fat tissue, which cannot be cleared by the dye.

### A. Tissue Clearing by Absorbing Dye Enables Increased Penetration Depth in OCT

We performed *in vivo* OCT imaging of pigmented and non-pigmented mice before and after topical application of either 4-aminoantipyrine or tartrazine to the abdominal skin. Cross-sectional OCT B-scan images of the pigmented mouse are shown in Figs. 2(a)–2(c). The baseline OCT B-scan of the pigmented mouse [Fig. 2(a)] revealed skin structure from the epidermis to dermis with substantial attenuation before reaching the subcutaneous tissue. This attenuation is likely caused by melanosomes and keratinocytes located in the epidermis of the pigmented mouse. OCT penetration depth was substantially improved in the pigmented mouse after applying 4-aminoantipyrine [Fig. 2(b)] and tartrazine [Fig. 2(c)]. In the B-scans of treated mice, structures from the epidermis to the muscle layer beneath the subcutaneous tissue layer become visible. We observed similar results in nonpigmented mice before and after treatment with the dye solutions, as depicted in Figs. 2(d)–2(f). The lack of melanin in the nonpigmented mice enabled OCT imaging to penetrate through the epidermis to the surface of the muscle beneath the skin, as shown in Fig. 2(d). After tissue clearing, OCT imaging was able to penetrate even deeper into the muscle and beyond. We observed a more detailed muscle structure with clearly defined fascia in the mouse treated with tartrazine [Fig. 2(f)] compared to the mouse treated with 4-aminoantipyrine [Fig. 2(e)].

Next, we took a closer look at the detail in the depth-enhanced OCT images made possible by tissue clearing. Figure 3(a) shows an enlarged view of the depth-enhanced OCT B-scan of the nonpigmented mouse treated with tartrazine. We validated the skin layer structure observed with depth-enhanced OCT with an image from a hematoxylin and eosin (H&E)-stained paraffin-embedded abdominal skin sample from wild type BALB/c mouse [18]. Figure 3(b) depicts the magnified view of the dashed green box in Fig. 3(a) highlighting the skin layers, and Fig. 3(c) shows an H&E-stained image of mouse abdominal skin found in the literature. The H&E image revealed the same structures observed in OCT including the epidermis, dermis, intradermal fat, and muscle. In the muscle layer, we observed clear striation patterns representing muscle fascia. The B-scan in Fig. 3(d) shows a depth-enhanced OCT B-scan from a pigmented mouse treated with 4-aminoantipyrine. A magnified view of the dashed orange box in Fig. 3(d) is shown in Fig. 3(e), which highlights hair follicles indicated by the yellow arrows in Fig. 3(e). A magnified view of the of the dashed blue box in Fig. 3(d) is shown in Fig. 3(f), which highlights hyperreflective foci located in the intradermal fat layer. These foci could be due to scattering by the nuclei of adipocytes.

To assess the time course of dye penetration, we performed OCT imaging prior to and at several time points following dye application in the region highlighted by the dashed green box in Fig. 1(a). Baseline OCT B-scan images [Fig. 4(a)] revealed skin structure from the epidermis to dermis with substantial attenuation before reaching the subcutaneous tissue. Shortly after the dye begins absorbing, structures beneath the skin surface become visible in the OCT B-scans. Figures 4(b)–4(g) depict B-scan images following dye application at 1, 5, 10, 15, 20, and 30 min, respectively. After 20 min [Fig. 4(f)], the dye is fully absorbed into the skin and structures from the epidermis to the muscle layer beneath the subcutaneous tissue layer become visible. To draw further comparison, we extracted intensity line profiles from dashed red and green lines in Fig. 4(a) and Fig. 4(f), respectively, and plotted

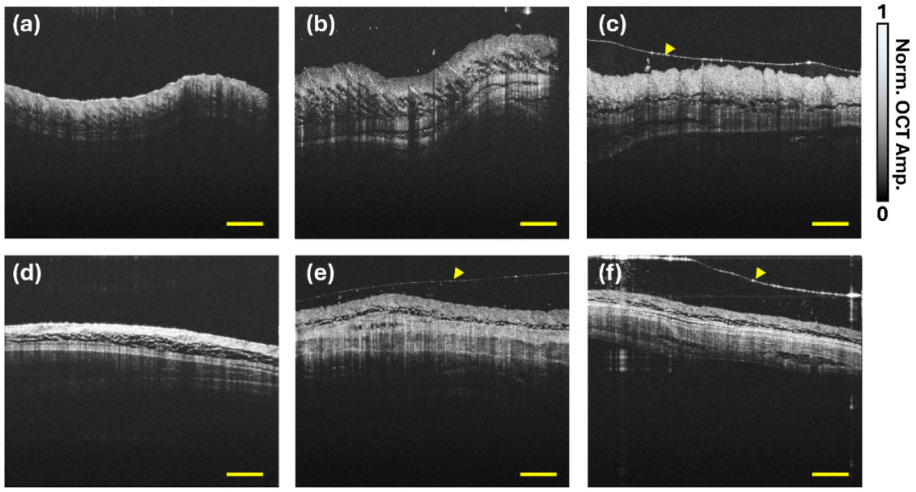


**Fig. 2.** Comparison of OCT B-scan images in pigmented vs. nonpigmented mouse using 4-aminoantipyrine and tartrazine. (a)–(c) OCT B-scan image of pigmented mouse abdomen before (a) and after treatment with 4-aminoantipyrine (b) and tartrazine (c). (d)–(f) OCT B-scan image of nonpigmented mouse abdomen before (d) and after treatment with 4-aminoantipyrine (e) and tartrazine (f). Scale bars: 500 μm. Yellow arrows indicate the surface of the topical tissue clearing solution.

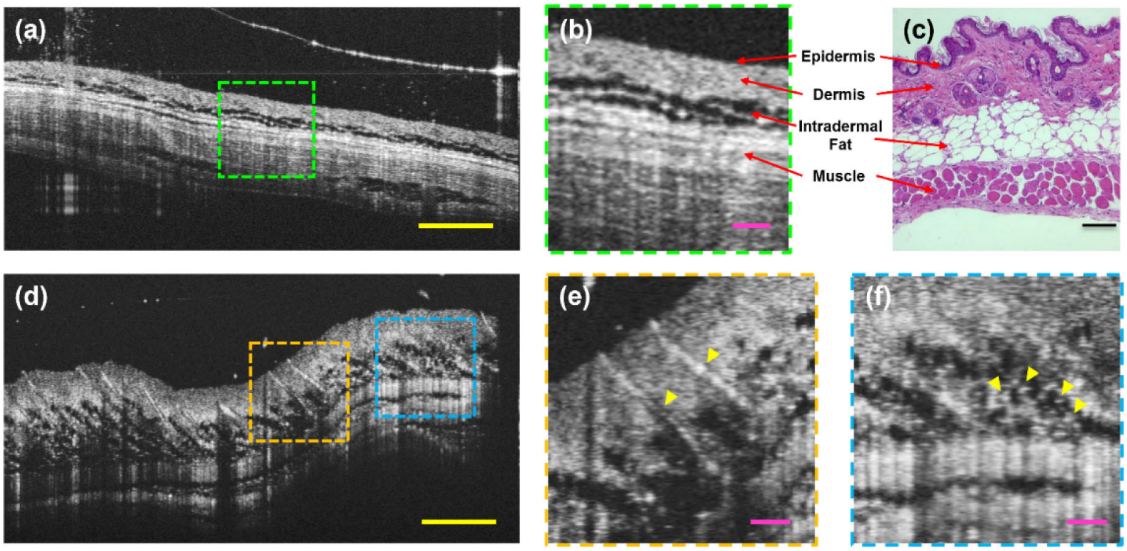


**Fig. 3.** Histological comparison of OCT images. (a) OCT B-scan image of nonpigmented mouse skin after applying tartrazine. (b) Enlarged view of region enclosed by dashed green box in (a). (c) H&E-stained paraffin-embedded abdominal skin sample from wild type BALB/c mouse [18]. (d) OCT B-scan image of pigmented mouse treated with 4-aminoantipyrine. (e) Enlarged view of region enclosed by dashed orange box in (d). Yellow arrows denote hair follicles beneath the skin surface. (f) Enlarged view of region enclosed by dashed blue box in (d). Yellow arrows denote possible adipocyte nuclei located in the intradermal fat layer. Scale bars: 500 μm (yellow), 100 μm (magenta and black).

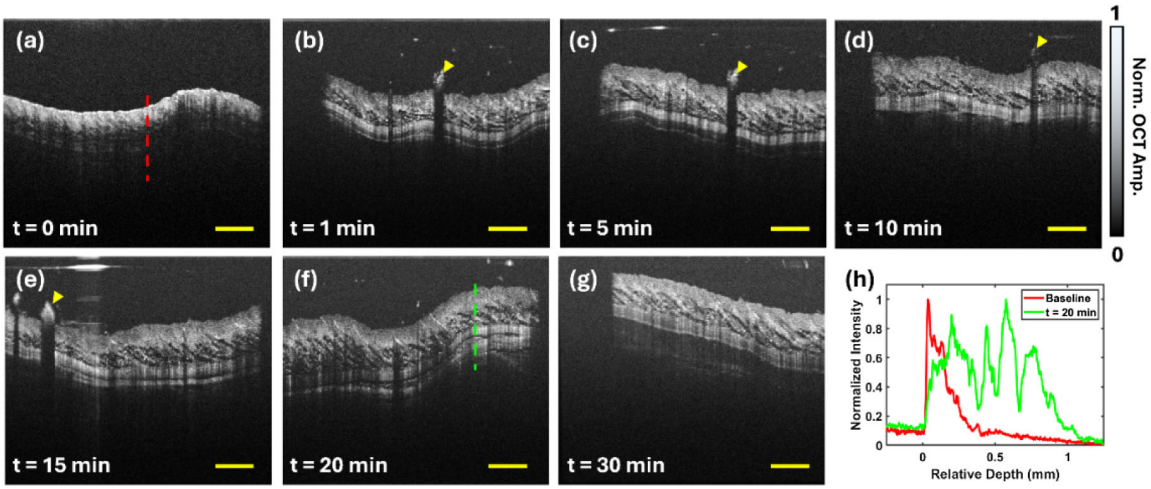


**Fig. 4.** OCT time course imaging of pigmented mouse abdominal skin before and after topical application of 4-aminoantipyrine. (a)–(g) OCT B-scan images of mouse abdominal skin before (a) and 1 min (b), 5 min (c), 10 min (d), 15 min (e), 20 min (f), and 30 min (g) following dye application. (h) Plot of intensity line profile extracted from the dashed red line in (a) and dashed green line in (f). Scale bars: 500 μm. Yellow arrows indicate residual grains of pumice sand.

them in Fig. 4(h). The intensity line profiles reveal strong attenuation in the baseline image (red line) with a maximum penetration depth of ∼0.4 mm. After 20 min of dye absorption (green line), the structures are clearly visible up to a depth of ∼1.0 mm–a 150% increase in penetration depth. We observed a similar effect for 4-aminoantipyrine.

### B. 4-aminoantipyrine Improves PA Penetration Depth

To further examine the effects of the two tissue-clearing dyes, PA imaging was performed for quantitative analysis. Figure 5 illustrates the PA imaging results before and after topical application of 4-aminoantipyrine and tartrazine. Compared to the baseline maximum amplitude projection (MAP) image [Fig. 5(a)], the mouse treated with 4-aminoantipyrine [Fig. 5(b)] produced a noticeably improved PA signal. After treatment with 4-aminoantipyrine, the PAM images showed stronger PA signal intensity and more blood vessels, suggesting more photons were able to penetrate the tissue. This improvement is also evident in the corresponding cross-sectional PA images in Figs. 5(c) and 5(d). Figure 5(e) shows a comparison of the line profiles extracted from the dashed lines, labeled L1 and L2, in Figs. 5(a) and 5(b), respectively. These line profiles reveal a twofold increase in PA signal intensity after 4-aminoantipyrine application.

In contrast, as predicted by the Kramers–Kronig relations, the tartrazine proved ineffective for PA imaging with 532 nm excitation. Compared to the baseline MAP image [Fig. 5(f)], the nonpigmented mouse treated with tartrazine showed a very

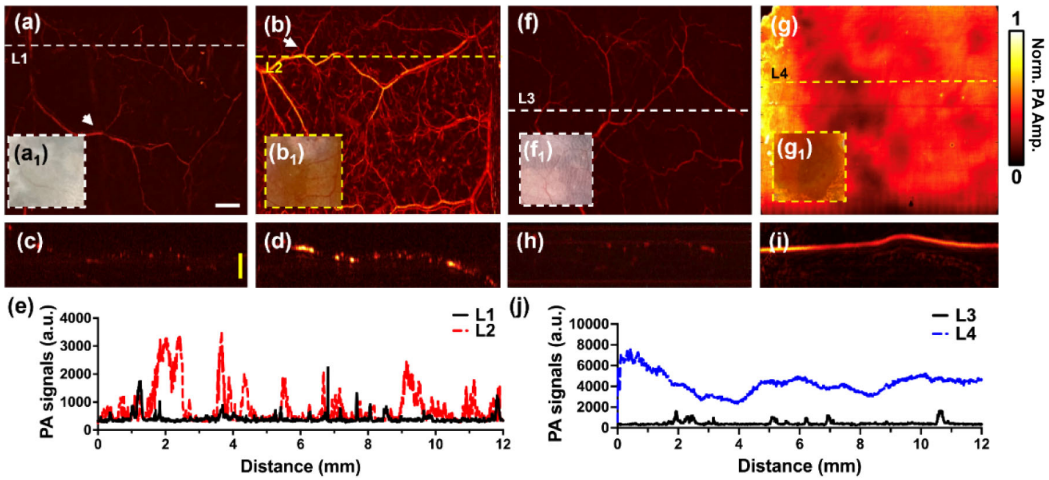


**Fig. 5.** PA imaging results. (a, b) Maximum amplitude projection (MAP) of PA images of mouse abdomen before (a) and after (b) applying 4-aminoantipyrine solution. ($a_1$) and ($b_1$) are photographs of the scanning region for (b) and (c), correspondingly. The white arrow indicates a matching blood vessel in (a) and (b). (c, d) Cross-sectional PA images before (c) and after (d) application of dye solution corresponding to the dashed lines in (a) and (b), respectively. (e) Line profile extracted from the dashed lines in (a) and (b), L1 and L2, respectively. (f, g) MAP of PA images of mouse abdomen before (f) and after (g) applying tartrazine solution. ($f_1$) and ($g_1$) are photographs of the scanning region for (f) and (g), correspondingly. (h, i) Cross-sectional PA images before (h) and after (i) application of dye solution corresponding to the dash lines in (f) and (g), respectively. (j) Line profile extracted from the dashed lines in (f) and (g), L3 and L4, respectively. Scale bars: 1 mm (white), 0.5 mm (yellow).

strong PA signal from the dye [Fig. 5(g)]. This strong absorption by the dye at 532 nm prevented sufficient laser energy from penetrating deeper into the tissue and overwhelmed the PA signal from the blood vessels. The corresponding cross-sectional PA images [Figs. 5(h)–5(i)] shows a thick bright band on the surface of the skin in the cross-sectional image for the mouse treated with tartrazine. A comparison plot of the line profiles extracted from the dashed lines in Figs. 5(f)–5(g) is shown in Fig. 5(j). The intensity line profile reveals an elevated signal from the mouse treated with tartrazine, with no discernible peaks indicating blood vessels.

## 4. DISCUSSION

We demonstrated the use of absorbing dye molecules to enhance the penetration depth of depth-resolved optical imaging modalities. In OCT images, the absorbing dye molecules, 4-aminoantipyrine and tartrazine, significantly increased the penetration depth beyond the dermis into the muscle in both pigmented and nonpigmented mice *in vivo*. Histological comparison confirmed the structures observed in the OCT images. Longitudinal imaging with OCT over 30 min indicated increased penetration depth as the dye was absorbed into the tissue. In PAM images, we observed increased penetration for the mouse treated with 4-aminoantipyrine and no improvement after tartrazine treatment with 532 nm excitation beam, thus confirming the prediction by the Kramers–Kronig relations for the dyes.

Before dye application, we observed substantial OCT signal attenuation in skin of pigmented mice compared to the nonpigmented mice. This is due to the scattering by the higher concentration of melanin in the epidermis of the pigmented mice. This high degree of optical scattering by skin has limited the adoption of OCT in dermatology. After topical dye application, OCT penetration depth was substantially improved up to 150%. Further optimization of dye molecules and application protocols could lead to even greater penetration depths. Tissue clearing with these water-soluble absorbing dye molecules provides a less invasive alternative to tissue biopsy and could accelerate the adoption of OCT in dermatology.

Depth-resolved optical imaging methods rely on the penetration of light into tissue. In particular, OCT relies on the collection of backscattered light and primarily generates contrast from ballistically scattered photons. Multiple scattering within tissue prevents photons from reaching deeper microstructures and returning to the collection aperture [19,20]. The degree of optical scattering in tissue is determined by the RI contrast between the aqueous-based components and lipid- and protein-based components. Scattering in tissue can be controlled by altering the physical structure of the tissue through compression, stretching, dehydration, coagulation, UV irradiation, and cooling [2,21–23] However, applying such physical stresses to the tissue could result in tissue damage, which is undesirable for longitudinal *in vivo* imaging studies. Others have tried introducing chemical changes to reduce RI contrast by impregnating the tissue with chemical solutions, gels, and oils [13,24,25]. However, such methods introduce chemical species that interrupt the biological processes under observation. For example, high concentrations of OCAs such as glycerol, and propylene glycol, have been shown in chick embryos to cause vasoconstriction and even block blood vessels in the applied areas, thus causing ischemia and inhibiting the delivery of nutrients [26,27].

The use of OCAs for enhancing OCT and PAM penetration depth has been explored previously. Wang and Tuchin provide a review of the tissue clearing methods applied for *in vitro* and *in vivo* OCT imaging of the skin and gastrointestinal tract tissues [7]. Wang *et al*. achieved similar results to those we present here after topically applying 80% glycerol solution to rat skin [7]. In another study, they used OCT to track the time course of glycerol absorption in porcine stomach tissue [28]. While these studies demonstrated the power of OCAs for enhancing OCT penetration depth, they did not provide a clinically suitable method for achieving tissue transparency due to the side effects of the OCA. For glycerol to increase the real component of the RI to that of water, the concentration must be very high, which results in dehydration

and shrinkage of tissue [6,7,25]. Sudheendran *et al*. achieved enhanced penetration depth using glucose solutions to perform OCT imaging of *ex vivo* porcine skin [26]. However, the introduction of glucose may influence the metabolic processes of the tissue.

The Lorentz oscillator model and Kramers–Kronig relations predict tissue clearing properties of dye molecules [6]. The center wavelength and amplitude of the molar absorption coefficient ($\alpha$) determines the molar change in the real component of the RI ($\beta$) for a given dye by the Kramers–Kronig relations. The optimal dye for a given imaging wavelength is one that increases the RI of aqueous components to match that of lipids and proteins at a concentration that is both low and physiologically tolerable [6]. The absorption peak of tartrazine is centered at 428 nm with a high $\alpha$ value. Thus, for PAM with an excitation wavelength of 532 nm, there is a strong increase in the RI of aqueous components beyond that of lipids and proteins. Based on the absorption spectrum of tartrazine and the Kramers–Kronig relations, we predict that a PAM system operating at wavelengths >600 nm would show better penetration depth than the 532 nm system we present here. On the other hand, 4-aminoantipyrine has an absorption peak centered at 380 nm with a lower $\alpha$ value than tartrazine. This results in a more modest increase in the aqueous RI at 532 nm, thus achieving better tissue clearing and PAM penetration depth. For OCT imaging at 840 nm, the RI of the tissue's aqueous component after treating with 4-aminoantipyrine or tartrazine is only moderately increased over that of pure water. To achieve better tissue clearing performance for OCT imaging at 840 nm, dye molecules with absorption peaks at longer wavelengths closer to 800 nm should be selected.

Hemoglobin has been explored previously for tissue clearing [29,30]. Heme exhibits intense absorption near 400 nm, which increases the refractive index of water at longer wavelengths when dissolved. However, its lingering absorption at these longer wavelengths means that absorption becomes significant as scattering decreases, making hemoglobin unsuitable for achieving transparency despite the reduction in scattering. In contrast, tartrazine and 4-aminoantipyrine display sharp absorption in the blue/UV region, effectively increasing the refractive index at longer wavelengths without introducing additional absorption, which is key to achieving transparency at these wavelengths.

Techniques for improving deep tissue imaging with OCT have been demonstrated previously. We introduced dual-axis OCT (DA-OCT) to enable deep tissue imaging using an off-axis illumination/detection configuration to collect multiply scattered photons from greater depths [31–33]. Using this technique, we achieved a penetration depth of 2.5 mm beneath the skin surface. Similarly, Untracht *et al*. introduced spatially offset OCT (SO-OCT) for deep tissue imaging and demonstrated significantly improved penetration depth in zebrafish and bone compared to conventional OCT [34]. Liba *et al*. demonstrated the use of speckle modulation by a ground glass diffusor to reduce speckle noise in OCT images of skin, which improved the resolution of deep tissue structures such as tactile corpuscles [35]. Tissue clearing using absorbing dye molecules makes it possible to perform deep tissue imaging without the need for complicated imaging setups or alternative acquisition protocols, which makes it simpler to implement on any OCT system. Further, combining these deep tissue imaging methods with tissue clearing by absorbing dye molecules could push the penetration depth of these techniques even deeper.

## 5. CONCLUSION

Water-soluble, absorbing dye molecules, like 4-aminoantipyrine and tartrazine, enhance the penetration depth of depth-resolved optical imaging techniques, such as OCT and PAM. Our results show the selection of the optimal dye molecules for a specific imaging wavelength is essential for maximizing optical penetration. Future studies will be targeted toward selecting the optimal dye and application protocol for a given imaging wavelength to push optical penetration even deeper, as well as examining the safety of the dyes for clinical use. The tissue clearing capabilities of biocompatible absorbing dye molecules enhances the diagnostic power of OCT and PAM, thus potentially accelerating their translation in clinical areas where adoption has been slow, such as dermatology.

**Funding.** National Institutes of Health (R01AG072732, RF1NS115581, R01NS111039, R01DK139109); National Science Foundation (2144788, CBET 2144788); Eli Lilly and Company; Chan Zuckerberg Initiative.

**Disclosures.** DAM: Lumedica Vision, Inc. (C), WJB: Lumedica Vision, Inc. (I, E). AW: Lumedica Vision, Inc. (I).

**Data availability.** Data underlying the results presented in this paper are not publicly available at this time but may be obtained from the authors upon reasonable request.

**Supplemental document.** See Supplement 1 for supporting content.

## REFERENCES

1. S. H. Yun and S. J. J. Kwok, "Light in diagnosis, therapy and surgery," Nat. Biomed. Eng. **1**, 0008 (2017).
2. V. V. Tuchin, *Optical Clearing of Tissues and Blood* (SPIE, 2006).
3. H. R. Ueda, A. Erturk, K. Chung, *et al.*, "Tissue clearing and its applications in neuroscience," Nat. Rev. Neurosci. **21**, 61–79 (2020).
4. K. Chung, J. Wallace, S. Y. Kim, *et al.*, "Structural and molecular interrogation of intact biological systems," Nature **497**, 332–337 (2013).
5. E. A. Susaki, K. Tainaka, D. Perrin, *et al.*, "Whole-brain imaging with single-cell resolution using chemical cocktails and computational analysis," Cell **157**, 726–739 (2014).
6. Z. Ou, Y. S. Duh, N. J. Rommelfanger, *et al.*, "Achieving optical transparency in live animals with absorbing molecules," Science **385**, eadm6869 (2024).
7. R. K. Wang and V. V. Tuchin, "Optical tissue clearing to enhance imaging performance for OCT," in *Optical Coherence Tomography* (Springer, 2015), pp. 1455–1487.
8. D. Huang, E. Swanson, C. Lin, *et al.*, "Optical coherence tomography," Science **254**, 1178–1181 (1991).
9. A. Alex, J. Weingast, B. Hofer, *et al.*, "3D optical coherence tomography for clinical diagnosis of nonmelanoma skin cancers," Imaging Med. **3**, 653–674 (2011).
10. S. Razi, Y. H. Kuo, G. Pathak, *et al.*, "Line-field confocal optical coherence tomography for the diagnosis of skin tumors: a systematic review and meta-analysis," Diagnostics **14**, 1522 (2024).
11. B. Wan, C. Ganier, X. Du-Harpur, *et al.*, "Applications and future directions for optical coherence tomography in dermatology," Br. J. Dermatol. **184**, 1014–1022 (2021).
12. J. Welzel, "Optical coherence tomography in dermatology: a review," Skin Res. Technol. **7**, 1–9 (2001).
13. X. Wen, S. L. Jacques, V. V. Tuchin, *et al.*, "Enhanced optical clearing of skin in vivo and optical coherence tomography in-depth imaging," J. Biomed. Opt. **17**, 066022 (2012).
14. J. J. Yao and L. H. V. Wang, "Photoacoustic microscopy," Laser Photon. Rev. **7**, 758–778 (2013).
15. M. Zafar, A. P. Siegel, K. Avanaki, *et al.*, "Skin imaging using optical coherence tomography and photoacoustic imaging: a mini-review," Optics **5**, 248–266 (2024).
16. Y. Zhou, J. J. Yao, and L. H. V. Wang, "Optical clearing-aided photoacoustic microscopy with enhanced resolution and imaging depth," Opt. Lett. **38**, 2592–2595 (2013).

17. M. V. Novoselova, T. O. Abakumova, B. N. Khlebtsov, *et al.*, "Optical clearing for photoacoustic lympho- and angiography beyond conventional depth limit," Photoacoustics **20**, 100186 (2020).
18. I. Kasza, Y. Suh, D. Wollny, *et al.*, "Syndecan-1 is required to maintain intradermal fat and prevent cold stress," Plos Genet. **10**, e1004514 (2014).
19. A. Wax and J. E. Thomas, "Measurement of smoothed Wigner phase-space distributions for small-angle scattering in a turbid medium," J. Opt. Soc. Am. A **15**, 1896–1908 (1998).
20. R. K. K. Wang, "Signal degradation by coherence tomography multiple scattering in optical of dense tissue: a Monte Carlo study towards optical clearing of biotissues," Phys. Med. Biol. **47**, 2281–2299 (2002).
21. I. F. Cilesiz and A. J. Welch, "Light dosimetry-effects of dehydration and thermal-damage on the optical-properties of the human aorta," Appl. Opt. **32**, 477–487 (1993).
22. E. K. Chan, B. Sorg, D. Protsenko, *et al.*, "Effects of compression on soft tissue optical properties," IEEE J. Sel. Top. Quantum Electron. **2**, 943–950 (1996).
23. I. Costantini, R. Cicchi, L. Silvestri, *et al.*, "In-vivo and ex-vivo optical clearing methods for biological tissues: review," Biomed. Opt. Express **10**, 5251–5267 (2019).
24. V. V. Tuchin, "Optical clearing of tissues and blood using the immersion method," J. Phys. D **38**, 2497–2518 (2005).
25. J. H. Lai, E. Y. Liao, Y. H. Liao, *et al.*, "Investigating the optical clearing effects of 50% glycerol in ex vivo human skin by harmonic generation microscopy," Sci. Rep. **11**, 329 (2021).
26. N. Sudheendran, M. Mohamed, M. G. Ghosn, *et al.*, "Assessment of tissue optical clearing as a function of glucose concentration using optical coherence tomography," J. Innov. Opt. Health Sci. **3**, 169–176 (2010).
27. D. Zhu, J. Zhang, H. Cui, *et al.*, "Short-term and long-term effects of optical clearing agents on blood vessels in chick chorioallantoic membrane," J. Biomed. Opt. **13**, 021106 (2008).
28. Y. H. He and R. Wang, "Dynamic optical clearing effect of tissue impregnated with hyperosmotic agents and studied with optical coherence tomography," J. Biomed. Opt. **9**, 200–206 (2005).
29. O. Sydoruk, O. Zhernovaya, V. Tuchin, *et al.*, "Refractive index of solutions of human hemoglobin from the near-infrared to the ultraviolet range: Kramers-Kronig analysis," J. Biomed. Opt. **17**, 115002 (2012).
30. V. V. Tuchin, D. M. Zhestkov, A. N. Bashkatov, *et al.*, "Theoretical study of immersion optical clearing of blood in vessels at local hemolysis," Opt. Express **12**, 2966–2971 (2004).
31. E. T. Jelly, Y. Zhao, K. K. Chu, *et al.*, "Deep imaging with 1.3 μm dual-axis optical coherence tomography and an enhanced depth of focus," Biomed. Opt. Express **12**, 7689–7702 (2021).
32. Y. Zhao, K. K. Chu, E. T. Jelly, *et al.*, "Origin of improved depth penetration in dual-axis optical coherence tomography: a Monte Carlo study," J. Biophoton. **12**, e201800383 (2019).
33. Y. Zhao, W. J. Eldridge, J. R. Maher, *et al.*, "Dual-axis optical coherence tomography for deep tissue imaging," Opt. Lett. **42**, 2302–2305 (2017).
34. G. R. Untracht, M. Z. Chen, P. Wijesinghe, *et al.*, "Spatially offset optical coherence tomography: Leveraging multiple scattering for high-contrast imaging at depth in turbid media," Sci. Adv. **9**, eadh5435 (2023).
35. O. Liba, M. Lew, E. SoRelle, *et al.*, "Speckle-modulating optical coherence tomography in living mice and humans," Nat. Commun. **8**, 15845 (2017).